Extreme Mechanics Letters 77 (2025) 102351

Contents lists available at ScienceDirect

Extreme Mechanics Letters

journal homepage: www.elsevier.com/locate/eml

Three-dimensional auxetic metamaterials with extremely tunable flexible behavior

Xiang Li [a,*], Weitao Peng [b], Rong Fan [c,*], Yang Lu [d,*]

[a] School of Science, Wuhan University of Science and Technology, Wuhan 430065, China
[b] School of Physics, Nanjing University of Science and Technology, Nanjing 210094, China
[c] Department of Mechanical Engineering, City University of Hong Kong, Hong Kong, China
[d] Department of Mechanical Engineering, The University of Hong Kong, Hong Kong, China

ARTICLE INFO

Keywords:
Auxetic metamaterials
Negative Poisson's ratio
Flexibility
Recoverability

ABSTRACT

Flexible auxetic metamaterials has demonstrated significant potential in engineering applications. However, most existing flexible auxetic metamaterials are limited to two-dimensional (2D) designs, restricting their utility in real 3D engineering scenarios. Here we represent a versatile strategy for designing 3D auxetic metamaterials that showcase extraordinary flexibility, recoverability, and programmability which is accomplished by embedding truss lattice with elastic spring into rotating rigid frameworks. We exemplify this approach with the eccentric spring connected rotating octet truss structures (ROCT-S) through experimental, numerical, and theoretical analysis. Under in-plane tension, engineering stress of the proposed eccentric spring connected rotating octet truss structures in two directions (ROCT-S-2D) is approximately 9.4×10^{-6} of the base material's modulus at an average strain of 161 %. Simultaneously, the programmable mechanical performance of the ROCT-S-2D under out-plane compression is decoupling with their in-plane performance and can be designed to support a load exceeding 12,800 times its own weight. The robust and adaptable mechanical performance of ROCT-S highlight its broad applicability, spanning electronics and biomedical devices to wearable flexible protective gear, paving the way for advanced 3D auxetic metamaterials in practical engineering solutions.

1. Introduction

Materials with negative Poisson's ratio (NPR), also known as auxetic materials, attract considerable attention due to their designable physical properties [1–3], such as rigid and compliant structures [4], shape programming [5], colossal magnetocaloric effect [6] and bending induced expansion [7], et al. Usually, auxetic materials were built by periodic regular structures [2,8], such as, re-entrant [9,10], chiral [11,12], missing ribs [13,14] and rotating rigid structures [15–17]. Dictated by their node connectivity, most of the classical auxetic structures are bending dominated structures with low stiffness and strength [18]. Therefore, these structures were used to design auxetic materials with low modulus, high stretchability, and low stress at large strains [18]. These materials can be named as flexible auxetic metamaterials and are commonly used as stretchable strain sensors [19,20], cardiac patches [21], triboelectric nanogenerator [22] and biomedical devices [23].

One effective strategy to design flexible auxetic metamaterials is transferring lattice's straight ribs into curved ones. Mechanical metamaterial with flexible behavior and large stretchability was obtained by replacing the straight microstructure in triangle lattices to horseshoe microstructure [24]. Theoretical analysis was conducted to given their stress–strain curves and Poisson's ratio [25]. A similar microstructure was employed in re-entrant and hexagonal lattice to achieve shape reconfigure, highly stretchability, and tunable Poisson's ratio [26]. Replacing the straight microstructure in triangular lattice to zigzag microstructure, the new lattice exhibits isotropic Poisson's ratio in the range from − 1 to 1 and controllable strain from 0 % to ~ 90 % [27]. Auxetic behavior and flexible performance were also found in the 2D structure with sinusoidally microstructure [28] as well as 3D lattice structures [29]. Chiral structure connected by curved microstructure exhibits tunable mechanical responses and high stretchability [30].

Another effective strategy to design flexible auxetic metamaterials is hierarchical design of the original auxetic structures. Usually, rotating rigid structures were used in this strategy [31–33]. High compressibility and stretchability, compression strain up to 0.5 and stretching strain up to 1.2, were obtained in hierarchical auxetic cellular materials [31].

* Corresponding authors.
E-mail addresses: xli@wust.edu.cn (X. Li), rongfan510@gmail.com (R. Fan), ylu1@hku.hk (Y. Lu).

https://doi.org/10.1016/j.eml.2025.102351
Received 6 December 2024; Received in revised form 19 April 2025; Accepted 28 April 2025
Available online 29 April 2025

Hierarchical design of rotating rigid squares could also increase its stretchability [32] or design metamaterials with shape configuration [32–35]. By changing geometry parameter of its microstructure, shape at a certain strain [32,33] or final shape [34,35] of the hierarchical metamaterials can be controlled. Most of the flexible auxetic cellular materials are 2D materials. However, true 3D structure brings more possibilities to mechanical metamaterials.

Some previous works reported auxetic metamaterials that can exhibit negative values for all the six on-axis Poisson's ratios [36], isotropic behavior [37,38], anisotropic behavior [39], tunable mechanical and conduction properties [40], and programming instabilities [41], in 3D spaces. It is still very challenging to develop 3D auxetic metamaterials that can reproduce flexible mechanical behavior at extreme large strains suggest potential uses in 3D engineering practices, for example, 3D biological tissues [42] and bio-integrated electronic devices [43].

In this work, through embedding connected truss lattices and springs into rotating rigid configuration, we develop a class of spring connected rotating truss lattice (RTL-S). First, spring connected rotating octet lattice in two directions (ROCT-S-2D) was fabricated and tested to show its auxetic behavior, excellent recoverability, extreme low Young's modulus, high flexible performance and tunable elastic properties under in-plane tension. Then, an analytical model was proposed to evaluate the elastic properties of the ROCT-S-2D with general connections. After that, spring connected rotating octet truss in three directions (ROCT-S-3D) were fabricated and tested to demonstrate their robust auxetic behavior, flexibility, and recoverability behavior. At last, two more 3D metamaterials with connected spring in two directions were fabricated and tested to demonstrate their decoupling mechanical performance under in-plane tension and out-of-plane compression as well as their programmable mechanical performance. Considering the outstanding mechanical properties of these metamaterials, it can be used in the area of electronic device, biomedical device as well as wearable protections.

2. Structural design

Traditional rotating rigid structures [15] follows the auxetic mechanism of the crystal structure [44] were often built by use of round [45], elliptical [16], rectangular [46] or even random [47] perforations into a planar structure. In their structures, the rigid structures and connections are built by bulk material. These limits their out-of-plane mechanical performance and in-plane deformability. 3D truss lattices could show programmable mechanical performance based on structural design. For example, octet structure (as shown in Figs. 1a and 1e) is one of the well-known truss lattices with high specific stiffness and stress. Springs, widely recognized as flexible structures, exhibit significant elastic deformation under low stress. Here, to integrate the auxeticity, flexible behavior, and programmable mechanical performance in one 3D structure, we proposed spring connected rotating octet truss structures (ROCT-S).

The first structure we create is ROCT-S-2D (Fig. 1c). In this structure, octet truss structure-1 (Fig. 1a) were connected by eccentric springs (Fig. 1b) in x and y directions. Here, eccentric spring were employed to prevent mutual interference. As illustrated in Fig. 1b, the eccentric spring is consisting by three parts: connect pillar, helix part and swirl part. Diameter of the eccentric spring and the octet truss structure-1 is D, length of the connect pillar is u, radius of the helix is R_1, pitch of the helix is p. The longer and shorter radii of the swirl part are R_0 and R_1, respectively. Therefore, the diameter of the swirl part is $R = \sin(\varphi/2)(R_1 - R_0) + R_0$. The second structure we create is ROCT-S-3D (Fig. 1f). Similar with the first structure octet truss and eccentric spring were also employed in this structure. Octet truss structure-2

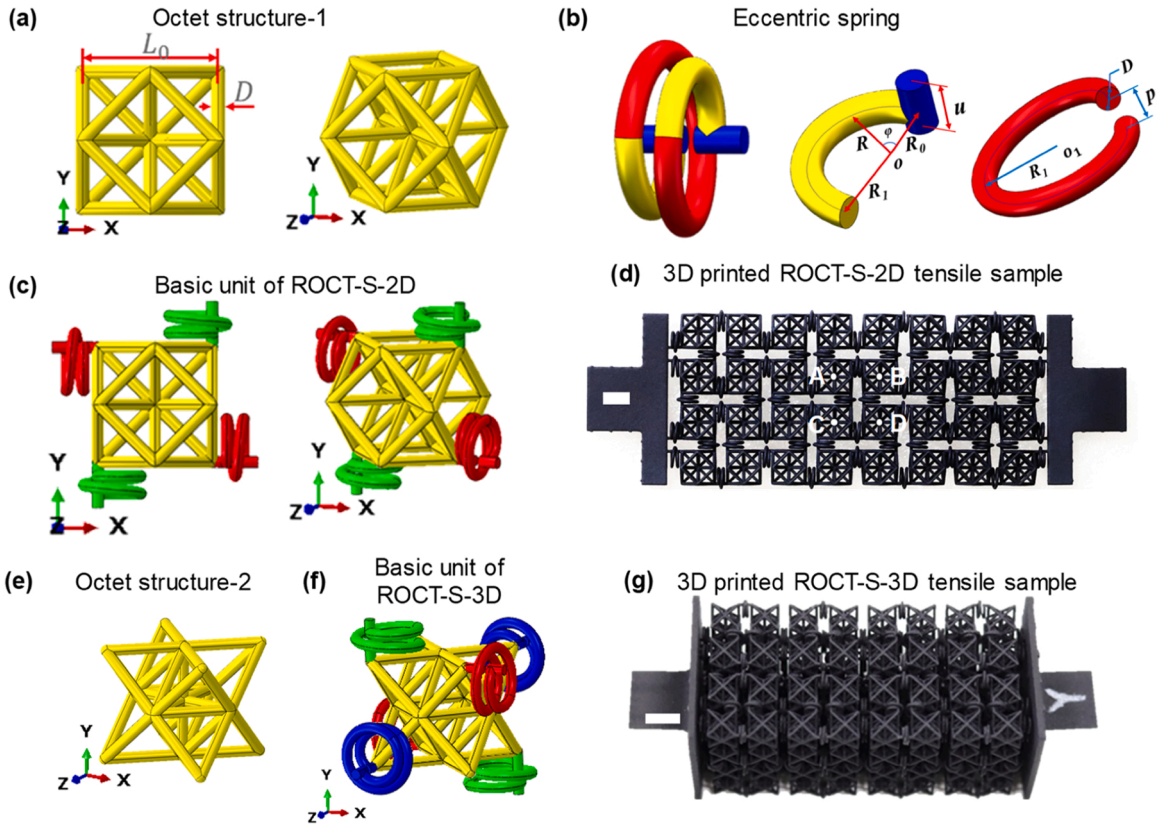

Fig. 1. Design and fabricated tensile samples of ROCT-S. (a) Octet structure-1, (b) eccentric spring, (c) basic unit of spring connected rotating octet truss in two-directions (ROCT-S-2D), (d) 3D printed ROCT-S-2D tensile sample, (e) octet structure-2, (f) basic unit of spring connected rotating octet truss in three-directions (ROCT-S-3D), (g) 3D printed ROCT-S-3D tensile sample. (Scale bars are 10 mm, four points in (d) was used to calculate the Poisson's ratio).

(Fig. 1e) was used in ROCT-S-3D, with its vertices connected in all three spatial directions via eccentric springs. Geometries eccentric spring used in ROCT-S-3D are the same with that used in the ROCT-S-2D. In the eccentric spring used in our 3D metamaterials, the helix spring only have one circle. While swirl spring connected with the helix spring have half of a circle in two sides. In addition, side length of the octet truss structure-1 and octet truss structure-2 is L_0.

3. Fabrication and mechanical test

3.1. Fabrication of the spring connected rotating truss lattice

ROCT-S-2D with base material of nylon was fabricated using 3D printing technology. In the ROCT-S-2D tensile samples, the total material contains 2×4 unit cells (see Fig. 1d). One layer and three layer compression samples with 2×2 unit cells were fabricated for the compression and load bearing tests (see Fig. S1). In these samples, D/L_0 was fixed as 0.1. While R_1/L_0 was changing from 0.25 to 0.4. In addition, tensile sample of ROCT-S-3D with $2 \times 4 \times 2$ unit cells was also fabricated using 3D printing technique (Fig. 1g). In this sample, D/L_0 and R_1/L_0 was 0.1 and 0.3 respectively.

3.2. Mechanical testing

Uniaxial in-plane tension tests were conducted using an MTS CMT6503 material testing system equipped with a 100 N load cell under displacement control. For out-of-plane compression tests, a 5KN load cell was employed. Since this study mainly focuses on the static mechanical behavior of the spring connected rotating truss lattice, a consistent loading rate of 1×10^{-4} was applied both in tension and compression experiments. A high-resolution canon camera (EOS 70D) was used to take pictures of the deformation progress during the tension tests every 10 s. Four points was marked in the middle of the tension samples to estimate the Poisson's ratio of the sample via digital image correlation method (Fig. 1d). Three samples were tested in the experiment to obtained the mechanical properties of the base materials (Fig. S2a).

4. Simulation and analytical models

4.1. Simulations of the spring connected truss lattices

To realize the mechanical behavior of the proposed metamaterials, mechanical behavior of spring-connected truss lattices was analyzed through simulations using commercial software ABAQUS. Three models were considered in the simulations. To obtain the elastic Young's modulus and Poisson's ratio under small strain of the ROCT-S-2D exactly, unit cell solid model with periodic boundary conditions (PBC) were performed in simulations (see Fig. 2a). In this simulation, finite element simulations (ABAQUS/static) with a 10-node quadratic tetrahedron C3D10 with 0.5 mm element size were performed. To obtain the tensile behavior of the ROCT-S-2D at large strain, multicellular beam model was used in simulations (see Fig. 2b). In this model, finite element simulations (ABAQUS/explicit) with a 3-node quadratic beam in space B32 with 0.5 mm element size were performed. Multicellular solid model (see Fig. 2c) was also considered in this paper to valid the multicellular beam model. Finite element simulations (ABAQUS/explicit) with a 10-node quadratic tetrahedron C3D10 with 0.5 mm element size were performed. General contact with 'hard contact' for the normal behavior and friction coefficient of 0.25 for the tangential behavior was performed in the multicellular beam and solid models. In all the simulations, the base material of the RTL-S was assumed to be elastic perfectly-plastic, and its corresponding Young's modulus and the Poisson's ratio is 900 MPa and 0.44, which was obtained in the tensile test of the base material. Stress-strain curves of the base material obtained in the test and used in the simulation were shown in Fig. 2d.

Stress-strain curves of the ROCT-S-2D obtained from the multicellular beam and solid models were shown in Fig. 2e. The corresponding Poisson's ratio was given in Fig. 2f. One can found that the stress-strain curves and corresponding Poisson's ratio obtained from the

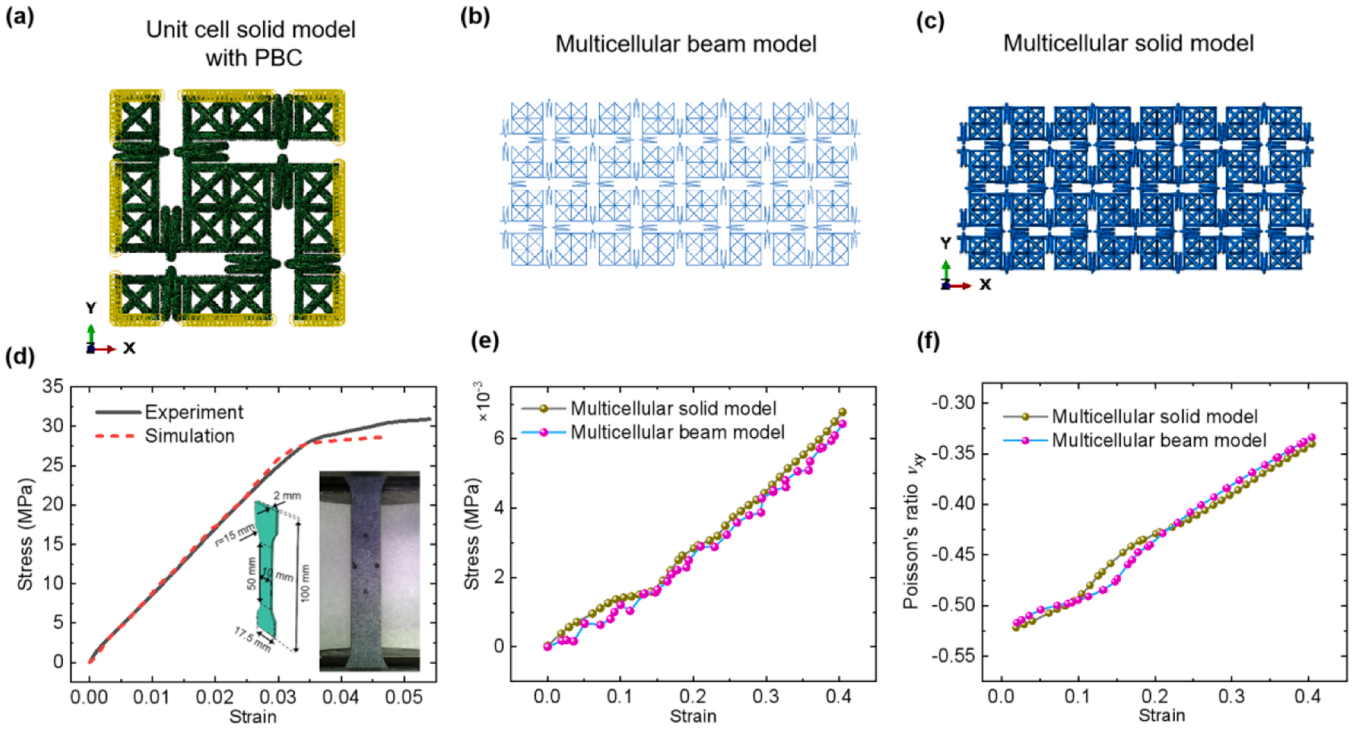

Fig. 2. Models and material properties used in the simulations. (a) Unit cell solid model of the ROCT-S-2D with periodic boundary conditions, (b) multicellular beam model and (c) multicellular solid model of the ROCT-S-2D used in the simulation, (d) stress-strain curves of the base materials, (e) stress-strain and (f) Poisson's ratio of the ROCT-S-2D obtained from simulations.

multicellular beam model agreed with that of multicellular solid model quite well. We consider structures with 1 × 2, 2 × 2, 2 × 3, 2 × 4, and 3 × 6 unit cells in the x and y directions (see Fig. S2b). The Poisson's ratio of the structure with 2 × 4 unit cells is about − 0.46. While, the Poisson's ratio obtained from the structure with 3 × 6 unit cells is − 0.43. The difference between the two results is less than 6 %. Considering the economic benefits, structures with 2 × 4 unit cells were used in the experiment in this paper.

4.2. Analytical model of spring connected octet truss lattice in two directions

To illustrate deformation mechanism of the ROCT-S-2D under in-plane tensile load, deformation of ROCT-S-2D with one unit cell were shown in Fig. 3. When a ROCT-S-2D unit cell was subjected to a tensile load 2F, the result force and moment applied on every octet truss was F and M, respectively. Similar with original rotating rigid squares, moment M would lead to rotate of the octet truss (see Fig. 3c). Resulting in expansion on the lateral direction of the ROCT-S-2D, i.e., negative Poisson's ratio. However, the force F would also lead to extension of the eccentric spring. Axial extension of the eccentric spring increases axial strain of the ROCT-S-2D. Therefore, the auxetic behavior of the ROCT-S-2D is lower than that of the rotating rigid squares.

For an ROCT-S-2D unit cell subjected to force 2F, the total moment applied on an octet truss is $M = FL_0$. Four eccentric springs were connected with one octet truss (see Fig. 3a). One can find that the force applied on eccentric springs A and B are F and 0, respectively. Assumed the corresponding moment applied on eccentric springs A and B are M_A and M_B, respectively (see Fig. 3b). Then, we have

$$2M_A + 2M_B = FL_0 \tag{1}$$

Assumed that the rotate angle of the eccentric spring under per unit moment is φ_0. The rotate angles of the eccentric springs A and B due to pure moment are

$$\varphi_A^M = M_A\varphi_0 \tag{2}$$

$$\varphi_B^M = M_B\varphi_0 \tag{3}$$

Rotate and stretch of the eccentric spring are coupling. Assumed that the rotate angle of the eccentric spring per unit force is φ_F. Then, the rotate angle of the eccentric spring A under force F is

$$\varphi_A^F = F\varphi_F \tag{4}$$

The deformation coordination requires that

$$\varphi_A^F + \varphi_A^M = \varphi_B^M \tag{5}$$

Solve Eqs. (1)–(5), the rotate angle of the eccentric spring B can be obtained:

$$\varphi_B^M = \frac{FL_0}{4}\varphi_0 + \frac{F}{2}\varphi_F \tag{6}$$

Rotate of the octet truss is shown in Fig. 3c. Rotate angle of the octet truss is $\varphi_B^M/2$. From the geometric relationship, displacement of a quarter of the ROCT-S-2D unit cell due to the rotate of the octet truss is

$$\delta^r = \frac{L_0}{2}\varphi_B^M = \frac{L_0FL_0}{8}\varphi_0 + \frac{FL_0}{4}\varphi_F \tag{7}$$

Assumed that the force constant of the eccentric spring is k_e. The elongation of the eccentric spring A due to pure tensile is

$$\delta_A^F = \frac{F}{K_e} \tag{8}$$

The displacement of the eccentric spring per unit moment is δ_b. Then, the elongation of the eccentric springs A and B due to moment are

$$\delta_A^M = M_A\delta_b = \frac{FL_0}{4}\delta_b - \frac{F}{2\varphi_0}\varphi_F\delta_b \tag{9}$$

$$\delta_B^M = M_B\delta_b = \frac{FL_0}{4}\delta_b + \frac{F}{2\varphi_0}\varphi_F\delta_b \tag{10}$$

Total displacements of the ROCT-S under axial and lateral directions are

$$\delta_{Axial} = \delta^r + \delta_A^M + \delta_A^F \tag{11}$$

$$\delta_{Lateral} = \delta^r + \delta_B^M \tag{12}$$

The axial and lateral stains of the ROCT-S are

$$\varepsilon_{Axial} = \frac{\delta_{Axial}}{(L_0 + L_r)} = \frac{\delta^r + \delta_A^M + \delta_A^F}{(L_0 + L_r)} \tag{13}$$

$$\varepsilon_{Lateral} = \frac{\delta_{Lateral}}{(L_0 + L_r)} = \frac{\delta^r + \delta_B^M}{(L_0 + L_r)} \tag{14}$$

where, L_r is the length of the eccentric spring (see Fig. 4b). The corresponding stress is

$$\sigma = \frac{F}{(L_0 + L_r)L_0} \tag{15}$$

Therefore, the Young's modulus of the ROCT-S-2D can be obtained

$$E = \frac{\sigma}{\varepsilon_{Axial}} = \frac{8K_e\varphi_0}{L_0\varphi_0K_eL_0(L_0\varphi_0 + 2\varphi_F + \delta_b) + 4L_0(2\varphi_0 - \varphi_F\delta_bK_e)} \tag{16}$$

While the corresponding Poisson's ratio is

$$\nu = -\frac{\varepsilon_{Lateral}}{\varepsilon_{Axial}} = -K_e\frac{L_0\varphi_0(L_0\varphi_0 + 2\varphi_F + \delta_b) + 4\varphi_F\delta_b}{L_0\varphi_0K_e(L_0\varphi_0 + 2\varphi_F + \delta_b) + 4(2\varphi_0 - \varphi_F\delta_bK_e)} \tag{17}$$

If the connection between the octet truss is an elastic mater without coupling between elongation and bending, then, the Young's modulus and Poisson's ratio of the ROCT-S-2D can be clarified as:

$$E = \frac{8K_e}{L_0(K_e/K_r + 8)} \tag{18}$$

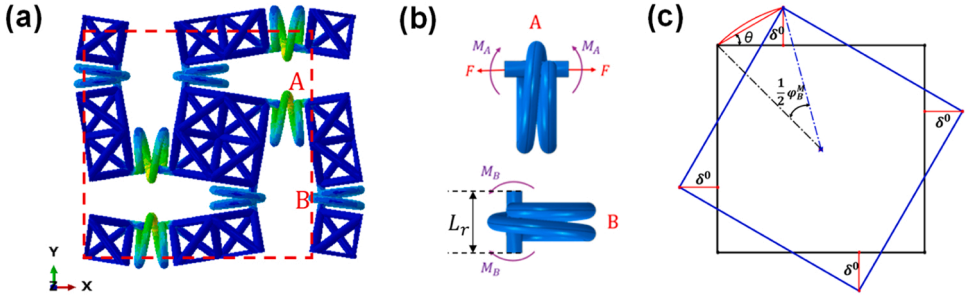

Fig. 3. Deformation and force analysis of the ROCT-S-2D. (a) Deformation of the unit cell of ROCT-S-2D, (b) force and moment applied on the eccentric springs A and B, and (c) rotate of the octet lattice under tension in direction x.

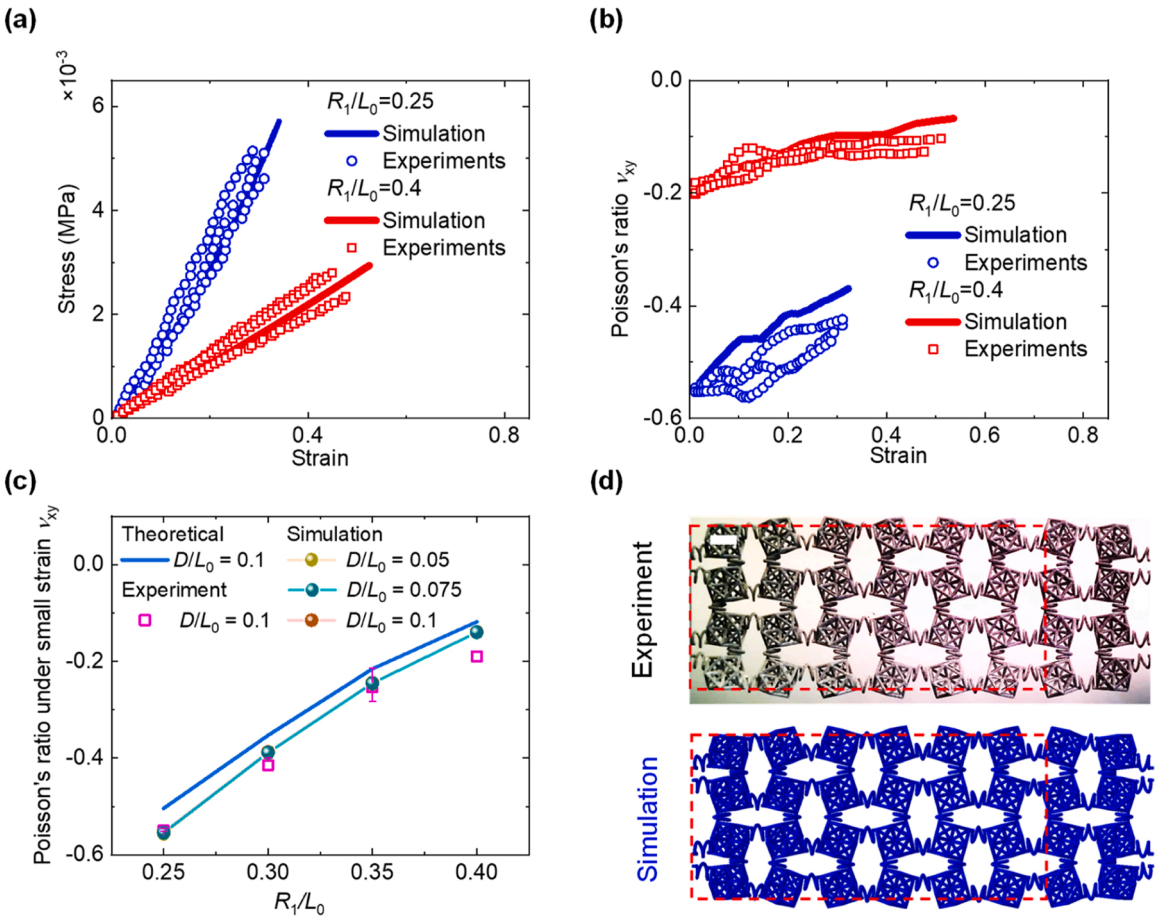

Fig. 4. Auxetic behavior of the ROCT-S-2D. (a) Stress-strain curves and (b) Poisson's ratio with different strain; (c) Poisson's ratio under small strain of ROCT-S-2D with different R_1/L_0; (d) deformation of the ROCT-S-2D obtained in experiments and simulation. (Scale bar 10 mm).

$$\nu = -\frac{K_e/K_r}{K_e/K_r + 8} \tag{19}$$

where, $K_r = 1/L_0\varphi_0 L_0$, is the rotate force constant of the connected matter. If $K_e = \lambda K_r$, from Eq. (18) we have $E = 8K_e/L_0/(\lambda + 8)$. Which means that for all $K_e = \lambda K_r$, effective Young's modulus E_0 has a linear relation with K_e.

Here, we try to give the Poisson's ratio of the ROCT-S-2D under small strain. Buckling and contact between springs occurs at large strains rather than small strain. Therefore, buckling and contact between springs were not considered in the theoretical model and Eqs. (16)–(19) can not be used at large strains. In addition, Eqs. (16) and (17) can be used to give the Young's modulus and Poisson's ratio of the structures with connections with coupling between elongation and bending, such as springs connections. While we also considered the connections without coupling between elongation and bending in Eqs. (18) and (19). These two equations can be used in a more simple connections, such as short struts connections.

5. Results and discussion

5.1. Auxetic behaviors of the ROCT-S-2D under in-plane tension

To illustrate the auxetic behavior of the ROCT-S-2D, in-plane tensile samples with $L_0 = 12.5$ mm and $D = 1.25$ mm were fabricated using 3D printing (Fig. 1d and S1a). Elastic behavior of the ROCT-S-2D is mainly dependent on the parameter of the eccentric spring and R_1/L_0. The stress-strain curves and Poisson's ratio ν_{xy} of ROCT-S-2D samples with $R_1/L_0 = 0.25$ and $R_1/L_0 = 0.4$ were shown in Figs. 4a and 4b. Three samples were used to obtain these results. As shown in Fig. 4a, the blue hollow circles represent the three stress-strain curves of the three ROCT-S-2D samples with $R_1/L_0 = 0.25$. One can find that the differences between the three tests were not significant, indicating the relative well reproducibility.

Poisson's ratio under small strain of the ROCT-S-2D with $D/L_0 = 0.1$ and different radius R_1/L_0 obtained from numerical and experimental methods was illustrated in Fig. 4b. One can find that the results obtained from these two methods agreed with each other quite well. As illustrated in Fig. 4b, the Poisson's ratio ν_{xy} of ROCT-S-2D increases with strain. Poisson's ratio under small strain ν_{xy} of the ROCT-S-2D with $R_1/L_0 = 0.25$ was about -0.55. After being stretched to 0.3 average strain, the Poisson's ratio ν_{xy} increases to a value of approximately -0.45 (Fig. 4b). In fact, the NPR behavior of this structure is induced by the rotate of the OCT structure. As shown in Fig. 3a, there is a spring connection on the left and right sides of the OCT structure. The spring generates a couple on the OCT structure to make it rotate. At small strain, the moment arm of the couple is L_0, the OCT structure can be rotate easily. Which leads to large NPR behavior of the whole structure. With the strain increase, the moment arm of the couple is decreased due to the rotate of the OCT structure, leading to the reduce of the NPR behavior of the whole structure. Stress-strain curves and Poisson's ratio ν_{xy} of ROCT-S-2D with $R_1/L_0 = 0.3$ and $R_1/L_0 = 0.35$ was illustrated in Fig. S3. Auxetic behavior was observed in these two samples under in-plane tension either.

To show the auxetic behavior clearly, deformation of the ROCT-S-2D at tensile strain $\varepsilon = 0.3$ obtained from experiment and simulation was illustrated in Fig. 4d. Where, a red rectangle was used to realize the boundary of the ROCT-S-2D before stretching. The simulation results

showed excellent agreement with experimental measurements, demonstrating lateral expansion characteristic of auxetic behavior. More deformation of the ROCT-S-2D samples under in-plane tension was shown in Fig. S4. Auxetic behavior can be observed in the tensile of all the samples even when the applied tensile strain up to 1.56.

Poisson's ratio at small strain of the ROCT-S-2D with different D/L_0 obtained from simulate, experimental and theoretical methods were given in Fig. 4c. With increase of R_1/L_0, the stiffness of the spring would be decrease. Resulting in the increase of the Poisson's ratio under small strain. When R_1/L_0 increase to 0.4, the corresponding Poisson's ratio under small strain increase to a value approximately − 0.2 (see Fig. 4c).

5.2. Recoverability of the ROCT-S-2D

To have a comprehensive understanding of the recoverability of the ROCT-S-2D, samples with R_1/L_0 equals to 0.25, 0.3, 0.35, and 0.4 were stretched four times. The preset stretched strain for the ROCT-S-2D is depend on R_1/L_0. For ROCT-S-2D with R_1/L_0= 0.25, the preset stretched strains for the first, second, and third time are 0.3, 0.4, and 0.5, respectively. While, for ROCT-S-2D with R_1/L_0= 0.4, the preset stretched strains are 0.55, 0.75, and 1, respectively. For the fourth time, all the samples are stretched to fracture. Stress-strain curves of ROCT-S-2D with R_1/L_0= 0.4 under this four times load was shown in Fig. 5a. Stress-strain curves obtained from four different times agreed each other very well. Negative Poisson's can be observed in this four times stretch. Detail stress-strain curves and Poisson's ratio of ROCT-S-2D under this four times stretch were given in Figs. S5 and S6.

Fig. 5b illustrate the recoverability of the ROCT-S-2D under in-plane tension. ROCT-S-2D with R_1/L_0= 0.25, can recover about 99 %, after stretched to 0.3. Increase the preset stretched strain to 0.5, the ROCT-S-2D with R_1/L_0= 0.25 can still have a recover up to about 97 %. Recoverability of the ROCT-S-2D is increase with R_1/L_0. When R_1/L_0 increase to 0.4, the recoverability at preset stretched strain 0.55 is approximately 99 %. Even when stretched for a strain up to 1, it can exhibit a high recoverability up to about 96 %. Recoverability of the ROCT-S-2D obtained in the tests was measured 30 minutes after the load is released. It should be noticed that the ROCT-S-2D can exhibit very large deformation ability. Fracture strain of the ROCT-S-2D was shown in Fig. 5c. The ROCT-S-2D can bear a large strain before fracture. The fracture strain of the ROCT-S-2D samples with R_1/L_0 equals to 0.25, 0.3, 0.35, and 0.4 is 0.6, 0.8, 1.1, and 1.4, respectively (see Fig. 5c). Figure of the ROCT-S-2D samples with R_1/L_0 equals to 0.25, 0.3, 0.35, and 0.4 after fracture was given in Fig. S4. One can find that the fracture mainly occurs at the spring connections. To demonstrate the robustness of its recoverability, ROCT-S-2D with R_1/L_0= 0.3 was stretched to 0.51 for 30 times. Recoverability of this structure under different loading times was given in Fig. 5d. This structure can recover about 98 %, after stretched to 0.51 for 5 times. Recoverability of the ROCT-S-2D is decrease with

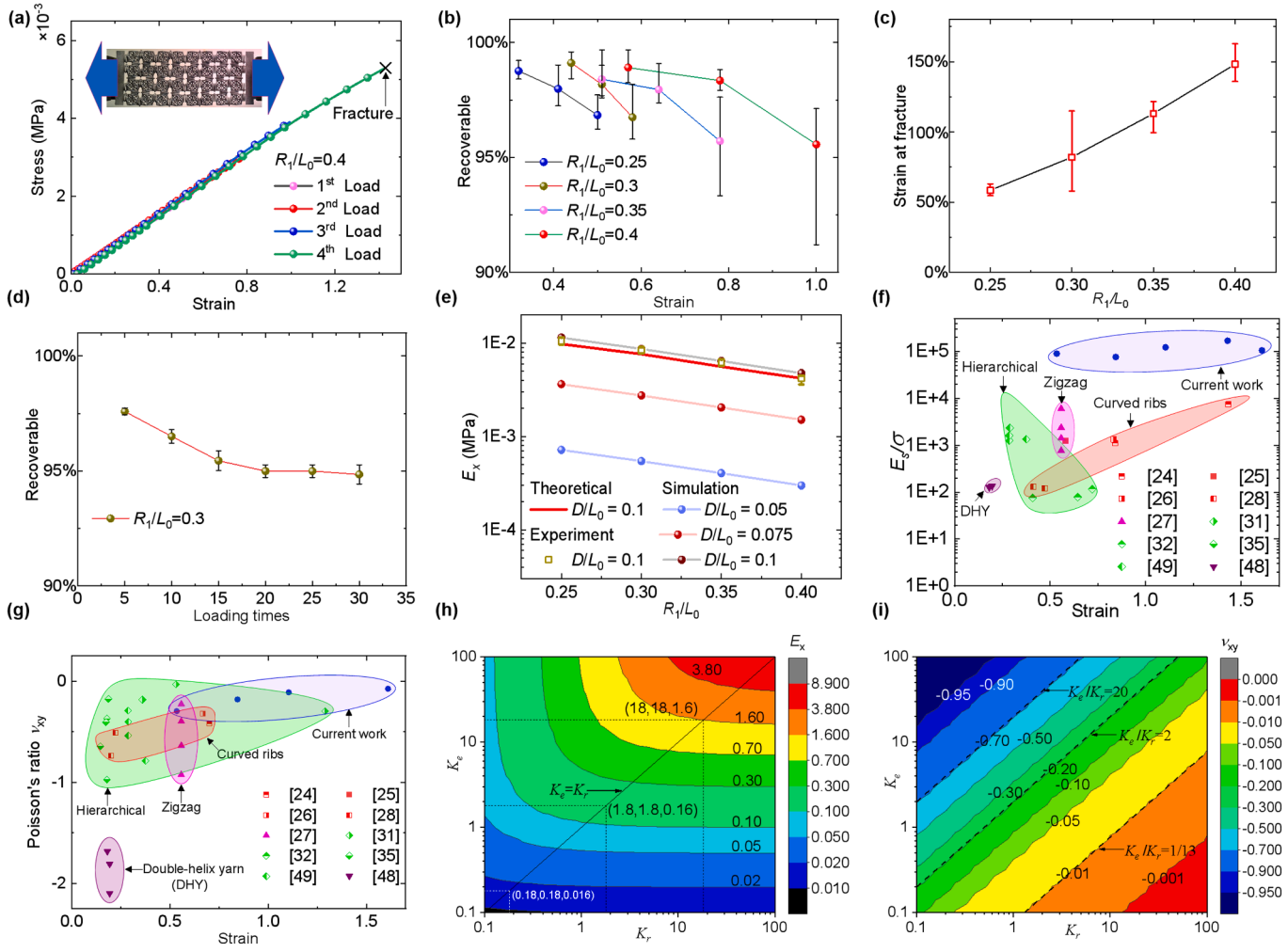

Fig. 5. Recoverability, flexible behavior and general elastic properties of ROCT-S-2D under in-plane tension. (a) Stress-strain curves, (b) recoverability, and (c) fracture strain of the ROCT-S-2D samples stretched four times; (d) recoverability of the ROCT-S-2D with R_1/L_0 = 0.3 under different loading times; (e) Young's modulus E_x of ROCT-S-2D; (f) E_S/σ and (g) Poisson's ratio of the ROCT-S-2D at different strains; (h) Young's modulus E_x and (i) Poisson's ratio under small strain ν_{xy} with different force constant of a general connection without coupling effect.

increase of loading times. However, the reduction rate gradually became smaller. Increase the loading times to 30, the structure can still have a recover up to about 94 %. This structure was also stretched to 0.3 for 50 times and the corresponding stress-strain curves obtained in the first, 20th, 40th, and 50th stretch was given in Fig. S7. We can see that the stress-strains in the 50th time was still very close to that of the first time, which indicate robust recoverability of ROCT-S-2D under cyclic load.

5.3. Extreme low Young's modulus and high flexible performance of the ROCT-S-2D under in-plane tension

Perhaps the most intriguing property of the ROCT-S-2D is their ability to exhibit extremely high flexible performance. First of all, ROCT-S-2D exhibit extremely low in-plane Young's modulus. This was benefit from the usage of spring as connections. We illustrated the effective Young's modulus of the ROCT-S-2D in Fig. 5e. The Young's modulus of the ROCT-S with $R_1/L_0 = 0.25$ was about 1.1×10^{-2} MPa (about 1.2×10^{-5} of its base material). Increase R_1/L_0 would reduce the stiffness of the spring and decrease in-plane modulus of the ROCT-S-2D. Increase R_1/L_0 to 0.4, the in-plane modulus of ROCT-S-2D reduced to about 4×10^{-3} MPa (about 4.4×10^{-6} of its base material).

As shown in Fig. 5e. With D/L_0 decrease, Young's modulus of the ROCT-S-2D will decrease. However, Poisson's ratio of the ROCT-S-2D with different D/L_0 is almost the same (see Fig. 4c). This indicating that the Young's modulus and Poisson's ratio of the ROCT-S-2D with different D/L_0 is independent as their Poisson's ratio is constant. If we want to design a ROCT-S-2D structure with specific values of Young's modulus E and Poisson's ratio ν, we can find a ROCT-S-2D structure satisfy the demand of auxetic behavior. Then, changing D/L_0 to obtain a structure with Young's modulus E we needed.

Secondly, our ROCT-S-2D structure can exhibit extreme high flexibility. Here, we use a normalized value E_s/σ to represent the flexibility of the structures. Where, E_s is the Young's modulus of the base material, and σ is the engineering stress of the auxetic metamaterials. For the same strain, materials with high value of E_s/σ indicate they have high flexibility. To have better comparison with the previous flexible auxetic materials, E_S/σ at large strains were given in Fig. 5f. Auxetic metamaterials built by the strategy with curved ribs [24–26,28], zigzag structure [27], double-helix yarn [48], and hieratical design [31,32,35,49] were included in this comparison.

As illustrated in Fig. 5f, E_s/σ of the zigzag auxetic material is about 5.9×10^3 at strain of approximately 0.56 [27]. However, E_s/σ of ROCT-S-2D is about 9.1×10^4 at the same strain, which is about 15.5 times of that of the zigzag auxetic metamaterial. For another example, E_s/σ of the curved ribs auxetic metamaterial is about 7.7×10^3 at strain of approximately 1.43 [24]. For ROCT-S-2D with $R_1/L_0 = 0.4$ at the same strain, the value of E_s/σ is about 1.7×10^5, 22 times higher than that of the curved ribs auxetic metamaterial. It's amazing to find that our spring connected truss lattices exhibit a flexibility one order higher than the previous flexible auxetic metamaterials. In another word, extreme high flexibility of our ROCT-S-2D means they could exhibit extreme low stress. For ROCT-S-2D with $R_1/L_0 = 0.4$, after stretched to a 161 % strain, its engineering stress was approximately 9.4×10^{-6} of the base material's modulus.

Last but not least, our ROCT-S-2D can exhibit auxetic behavior at very large strains. As we mentioned in the previous section, auxetic behavior of the ROCT-S-2D was decrease with the tensile strain. However, they can still exhibit auxetic behavior at very large strains. As illustrate in Fig. 5g, the Poisson's ratio of the ROCT-S-2D at strain of 0.54, 1.11, and 1.61 was approximately − 0.3, − 0.11, and − 0.08 respectively.

5.4. Elastic properties of the ROCT-S-2D with general connections

To have a better understanding of the elastic properties of the ROCT-S-2D, Young's modulus and Poisson's ratio with different K_e and K_r were given in Figs. 5h and 5i. Where, K_e and K_r are the stretching and rotate force constant of the eccentric spring. Here, L_0 is fixed as 10, while K_e and K_r are changing from 0.1 to 100. The effective Young's modulus of the ROCT-S-2D has a linear relation with force constant K_e when $K_e = K_r$ (Fig. 5h). For $K_e = K_r = 0.1$, the effective Young's modulus E_0 is about 8.9×10^{-3}. Increasing K_e and K_r to 100, the value of E_0 increases to 8.9 (see Fig. 5h). In fact, for all $K_e = \lambda K_r$, effective Young's modulus E_0 has a linear relation with K_e.

It should be noticed that the auxetic behavior of the ROCT-S-2D comes from the rotate of the octet truss under load. When the force constant K_e is much larger than the rotating force constant K_r, i.e., $K_e \gg K_r$, the octet trusses can be rotated easily, resulting in a large auxetic behavior of the ROCT-S-2D under in-plane tension (Fig. 5i). For example, when $K_e/K_r = 1000$, the Poisson's ratio is about − 0.99, a performance very close to ideal rotate rigid squares [15]. However, when $K_e \ll K_r$, rotate of the octet trusses is constrained. Resulting in near zero Poisson's ratio of ROCT-S-2D. For example, when $K_e/K_r = 1/13$, the Poisson's ratio is approximately − 0.01. This indicate that the Poisson's ratio of the ROCT-S-2D is only dependent on the ratio K_e/K_r. Therefore, similar with other auxetic metamaterials, the Poisson's ratio of the ROCT-S-2D is material and scale independent. In addition, the analytical results can also be used to illustrate the auxetic behavior of the auxetic structures with elliptical [16] or rectangular [46] perforations into a planar structure.

5.5. Tensile behavior of the ROCT-S-3D

Similar with the 2D situation, robust flexibility, recoverability and negative Poisson's ratio behavior were also observed in the tensile test of the ROCT-S-3D. Tensile sample of the ROCT-S-3D were shown in Fig. 1g. Cyclic tensile testing was performed on this sample for 25 cycles at 0.35 maximum strain. Stress-strain curves and corresponding Poisson's ratio for this sample when stretched for the first, 10th, and 25th load was given in Figs. 6a and 6b, respectively. The ROCT-S-3D also possess extreme low modulus. From the stress-strain curves in Fig. 6a, the Yong's modulus of the ROCT-S-3D is 4.5×10^{-3} MPa, which was about 5×10^{-6} of its base material. As illustrated in Fig. 6a, at the strain of 0.35, the stress for the first time was about 1.8×10^{-3} MPa. However, the stress for the 25th time load was about 1.7×10^{-3} MPa, which was very close to that for the first time. This indicates excellent recoverability for the ROCT-S-3D. Auxetic behavior can be found both in the first and 25th stretch of the ROCT-S-3D (see Fig. 6b). Though there is some differences between the first and 25th stretch. However, similar differences can be found in the Poisson's ratio of ROCT-S-2D with different samples (see Fig. 4b). Considering the calculation error, we believe the ROCT-S-3D exhibit similar auxetic behavior.

To have a clear observation of the auxetic behavior of the ROCT-S-3D, deformation of this structure was given in Fig. 6c. A yellow dash line was used to represent the original boundary of the ROCT-S-3D. When the ROCT-S-3D was stretched to a strain of 0.3, an obvious lateral expansion was observed in Fig. 6c, which indicate its auxetic behavior. Similar with the structure with spring connected in two directions, auxetic behavior of the ROCT-S-3D was also decrease with the applied strain. As shown in Fig. 6b, Poisson's ratio of ROCT-S-3D under small strain was about − 0.38. When stretching the ROCT-S-3D to a strain of 0.3, its Poisson's ratio increases to a value approximately − 0.31.

Young's modulus and Poisson's ratio under small strain of the ROCT-S-3D with different L_0/R_1 obtained from simulations were shown in Figs. 6d and 6e, respectively. Here R_1 and D is fixed as 3.25 mm and 1.25 mm, respectively. With L_0/R_1 increase the Young's modulus of the ROCT-S-3D decrease. Young's modulus of the ROCT-S-3D with $L_0/R_1 = 4$ is about 3.3×10^{-3} MPa. However, increase L_0/R_1 to 12, this structure's Young's modulus decreases to a value about 1.3×10^{-4} MPa (see Fig. 6d). Low modulus of the structure indicate that they can have higher flexibility. In should be noticed that ROCT-S-3D with higher flexibility

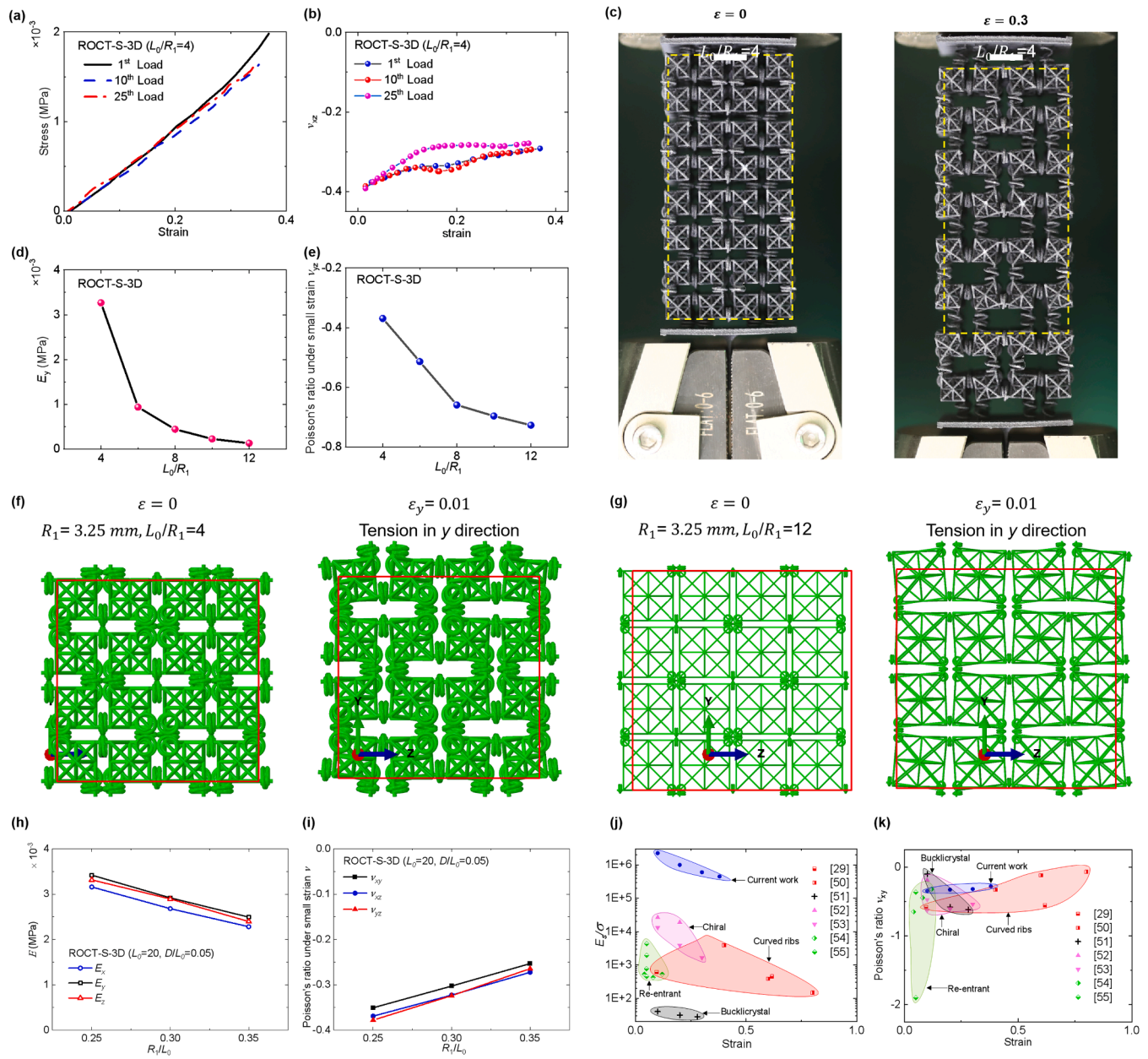

Fig. 6. Tensile behavior of the ROCT-S-3D. (a) Stress-strain curves, (b) Poisson's ratio and (c) deformation of the ROCT-S-3D with L_0/R_1= 4; (d) Young's modulus and (e) Poisson's ratio under small strain of the ROCT-S-3D with different L_0/R_1; (f)-(g) deformation of the ROCT-S-3D with L_0/R_1 equals to 4 and 12; (h) Young's modulus and (i) Poisson's ratio under small strain of the ROCT-S-3D in three orthogonal directions; (j) E_S/σ and (k) Poisson's ratio of the ROCT-S-3D at different strains. (scale bar in (c) is 10 mm).

could have large auxetic behavior either. For example, Poisson's ratio of ROCT-S-3D with $L_0/R_1 = 4$ is about − 0.4, while Poisson's ratio of ROCT-S-3D with $L_0/R_1 = 12$ is about − 0.7, a value much smaller than − 0.4. This makes it possible to design metamaterials with large auxetic behavior as well as extreme high flexibility. Deformation of the ROCT-S-3D with $L_0/R_1 = 4$ and $L_0/R_1 = 12$ was shown in Figs. 6f and 6g, respectively. Young's modulus and Poisson's ratios of the ROCT-S-3D in three orthogonal directions were given in Figs. 6h and 6i. Obviously, the Young's moduli of the ROCT-S-3D in three orthogonal directions were very close. Similar auxetic behavior can be found in this figure. Therefore, the ROCT-S-3D show similar mechanical performance in three orthogonal directions.

E_S/σ and Poisson's ratio of the ROCT-S-3D at different strains were compared with 3D auxetic structures in Figs. 6j and 6k. Here, 3D auxetic structures with curved ribs [29,50], bucklicrystals [51], chiral structures [52,53], and re-entrant structures [54,55] were used in this comparison. Similar with the situation in 2D structures, the ROCT-S-3D show extremely high flexibility than the previous 3D auxetic structures.

5.6. Anisotropic auxetic behavior of the RCDT-S-2D

The strategy we proposed to design flexible auxetic metamaterials in two and three directions can expand to other structures. Inspired by the rotate rigid rectangles [17], one can obtain spring connected rotating rectangular octet truss in two directions (RCDT-S-2D) (Fig. 7a). In this structure, rectangular octet trusses were connected by eccentric springs in x and y directions (Fig. 7a). L_x and L_y are length of the rectangular octet truss in x and y directions, respectively (Fig. 7a).

Auxetic behavior of the RCDT-S-2D with different L_x/L_y were shown in Figs. 7b and 7c. Here L_y and R_1/L_y were fixed as 12.5 mm and 0.3,

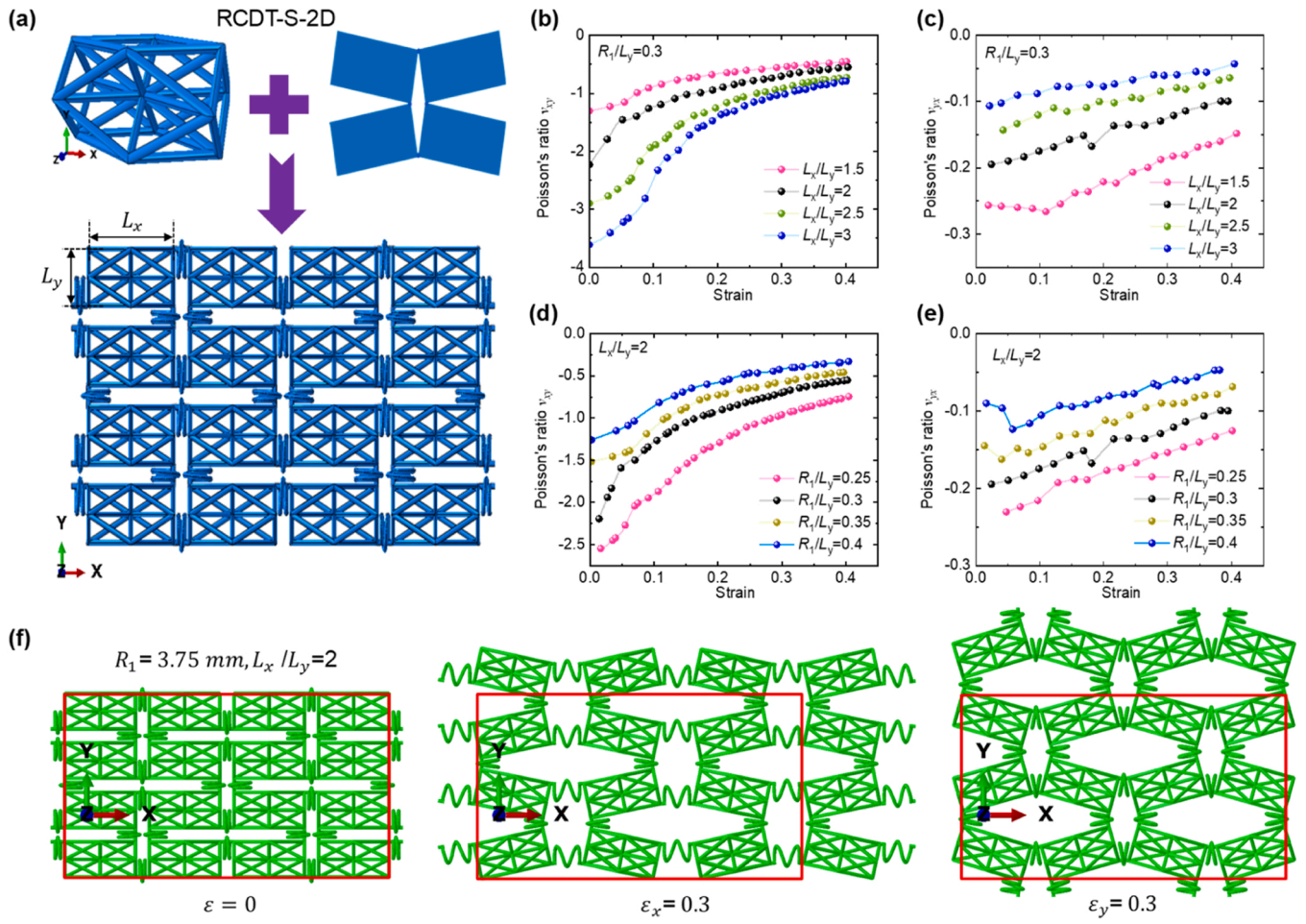

Fig. 7. Design and auxetic behavior of the RCDT-S-2D. (a) structure design, (b-e) Poisson's ratio and (f) deformation of the RCDT-S-2D. (Here D is fixed as 1.25 mm and L_y is fixed as 12.5 mm).

respectively. Large auxetic behavior can be observed when stretched in x direction. Poisson's ratio ν_{xy} at small strain of the RCDT-S-2D with L_x/L_y= 2 was about − 2.2 (Fig. 7b). While its Poisson's ratio ν_{yx} at small strain was about − 0.2 (Fig. 7c). To show the anisotropic auxetic behavior clearly, deformation of this structure was shown in Fig. 7f. Obvious lateral expansion in the y direction can be observed when the structure is stretched in x direction. However, lateral expansion was small when it was stretched in the y direction. Increase the aspect ratio L_x/L_y to 3, Poisson's ratio ν_{xy} and ν_{yx} at small strain of the RCDT-S-2D changed to − 3.6 and − 0.1, respectively. This indicate that the anisotropic of the structure increase with the aspect ratio L_x/L_y.

Auxetic behavior of the RCDT-S-2D with different R_1/L_y were shown in Figs. 7d and 7e. Here L_x/L_y is fixed as 2. Similar with the ROCT-S-2D, large auxetic behavior was observed in RCDT-S-2D structures with small R_1/L_y. Poisson's ratio ν_{xy} and ν_{yx} at small strain of the RCDT-S-2D with R_1/L_y = 0.25 is about − 2.6 and − 0.24, respectively. Increase R_1/L_y to 0.4, Poisson's ratio ν_{xy} and ν_{yx} at small strain changed to about − 1.25 and − 0.09, respectively.

Inspired by the rotate rigid triangles [15], spring connected rotating triangle truss in two directions (RTTS-S-2D) can be obtained (Fig. S8a). Young's modulus, Poisson's ratio and deformation of RTTS-S-2D under small strain was given in Fig. S8b–d. Anisotropic auxetic behavior was observed in the RTTS-S-2D under in-plane tensile load.

5.7. Programmable mechanical performance of RTL-S-2D under out-plane compression

Lattices used in RTL-S-2D can be regard as a black box, which can be replaced by architectures based on the demand of the real engineering application. Here we given two more spring connected rotating cube lattices in two directions. The first structure is spring connected reduced octet lattice in two directions, which is short for RCOTY-S-2D. Reduced octet lattice is reduced a 'X' structure vertical to the y direction in the octet structure. The second structure is spring connected re-entrant lattice in two directions, which is short for RREL-S-2D. Basic structures of the RCOTY-S-2D and RREL-S-2D were given in Fig. 8a. As illustrated in Fig. 8b, stress-strain curves of RREL-S-2D and RCOTY-S-2D obtained from experiment under in-plane tension was almost the same with that of ROCT-S-2D. In fact, their effective in-plane Young's modulus were about 1.2×10^{-2} MPa. However, out-of-plane compression behavior of these three structures was quite different (Fig. 8c). Effective Young's modulus of the ROCT-S-2D, ROCTY-S-2D, and RREL-S-2D subjected to out-of-plane compression were 14.6, 7.6, and 1.4 MPa respectively, which is about 1216, 633, and 116 times of the in-plane tensile Young's modulus. This indicates that the out-of-plane compression performance of RTL-S-2D are dependent on its cube lattice's structure rather than the connected springs, and can be designed based on the demand of the real engineering application. Resulting in the decoupling effect between the in-plane and out-plane mechanical performance, which bring more degrees of freedom in their mechanical performance.

We compared the normalized Young's modulus of the ROCT-S-2D

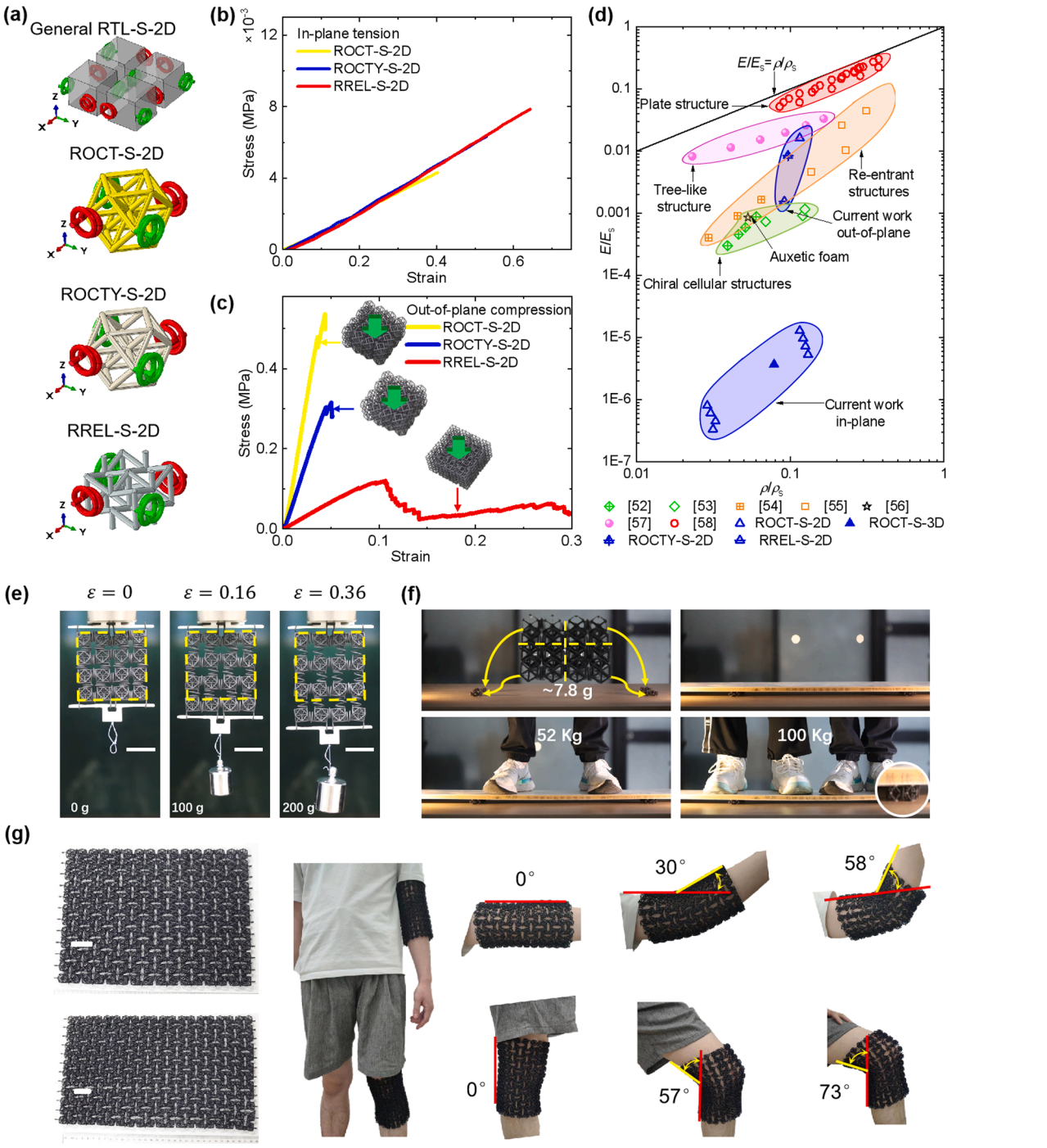

Fig. 8. General structure of the RTL-S-2D and their potential applications. (a) General structure of RTL-S-2D and their basic units; stress-strain curves of the RTL-S-2D under (b) in-plane tension and (c) out-of-plane compression; (d) E/E_s versus ρ/ρ_s of the ROCT-S-2D and ROCT-S-3D; load bearing of the ROCT-S-2D under (e) in-plane tension and (f) out-of-plane compression; (g) flexible protection application of the ROCT-S-2D. (scale bars in (e) and (g) are 30 mm).

and ROCT-S-3D with other 3D NPR cellular materials in Fig. 8d. E/E_s of chiral structures [52,53], and re-entrant structures [54,55], auxetic foam [56] were included in this figure. In addition, stretching-dominated tree-like structures [57] and plate structure with negative Poisson's ratio [58] were also included in this figure. From this figure, one can find that chiral structure show low modulus than other 3D NPR cellular materials. However, the modulus of the chiral structure is about 100 times higher than the ROCT-S-2D and ROCT-S-3D proposed in our manuscript. This proves extreme low Young's modulus of our ROCT-S-2D and ROCT-S-3D under in-plane tension. While the E/E_s of RTL-S-2D under out-of-plane compression could be similar with the re-entrant structure [54] or the stretching-dominated tree-like structures [57]. This demonstrates the designability of the out-of-plane modulus of RTL-S-2D over a wide range.

It should be notice that the eccentric spring used in this paper only has one helix coil and one swirl coil. Increase the number of coils, recoverability and flexibility of our 3D metamaterial will increase. Discovering, characterizing, fabrication and application of these 3D flexible auxetic metamaterials need more researchers' efforts.

5.8. Potential application of the RTL-S-2D

Previously we show that the mechanical performance of the ROCT-S-2D subject to in-plane tension and put-of-plane compression load are decoupling. Load bearing of the ROCT-S-2D subject to in-plane tension and put-of-plane compression were demonstrated in Figs. 8e and 8f. A one-layer ROCT-S-2D with 2×2 unit cells was used in this demonstration. When a ROCT-S-2D with 2×2 unit cells was bearing a 100 g and 200 g weight under in-plane tension load, the corresponding strain was approximately 0.16 and 0.36 (see Fig. 8e). However, the ROCT-S-2D could bear very large weight when it was under out-of-plane compression. As demonstrated in Fig. 8f, the weight of a ROCT-S-2D with 2×2 unit cells is approximately 7.8 g. We cut it into 4 pieces and let them to be the load-bearing structure. A plate board was covered on the one-layer ROCT-S-2D to supporting heavy objects. Two students with a weight of 100 Kg were stand on the plate board and the one-layer ROCT-S-2D was remained intact (see Fig. 8f). This proved that the ROCT-S-2D can withstand out-of-plane compressive loads exceeding 1.28×10^4 times its own weight.

Considering the extreme in-plane flexible behavior of RTL-S-2D and its programmable out-of-plane compression performance, we believe our RTL-S-2D can be used as wearable flexible protections. Fig. 8f showed the possibility to use ROCT-S-2D as wristband and kneepad. Depend on the size of arm and leg, ROCT-S-2D with different total sizes were fabricated. Then, the flat ROCT-S-2D were curved to a tube wearing on the arm and leg. The ROCT-S-2D-based wristband enabled arm flexion exceeding 58° while worn. While, the ROCT-S-2D-based kneepad allowed for leg flexion exceeding 73° during use. In addition, the auxetic behavior of the ROCT-S-2D leads to small warp of the ROCT-S-2D based wristband and kneepad when the arm and leg is bending. This makes the ROCT-S-2D wristband and kneepad more comfortable.

6. Conclusion

In summary, we report a universal strategy to design 3D flexible auxetic metamaterials with extreme flexible performance by introducing truss lattice and eccentric spring in rotating rigid frameworks. To demonstrate the broad applicability of our design strategy, we propose and investigate six additional 3D flexible auxetic metamaterials: ROCT-S-2D, ROCT-S-3D, ROCTY-S-2D, RREL-S-2D, RCDT-S-2D, and RTTS-S-2D.

The ROCT-S-2D structure demonstrate three key characteristics: (1) exceptional in-plane tensile flexibility, (2) high recoverability, and (3) programmable mechanical properties, while maintaining negative Poisson's ratio behavior. A general analytical method has been proposed to characterize the auxetic behavior and Young's modulus of the ROCT-S-2D under in-plane load. The ROCT-S-3D structure exhibited auxetic behavior, high recoverability and demonstrating exceptional in-plane tensile flexibility along three orthogonal directions. The RTL-S-2D can exhibit extreme low modulus under in-plane tension and withstands huge loads under out-of-plane compression. Independence of in-plane and out-of-plane performance and the decoupling of elastic modulus and Poisson's ratio of the RTL-S-2D greatly improves the designability of these structures. This study opens up new avenues for the design and fabrication of novel 3D auxetic metamaterials experiencing ultra-flexible behaviors. We expect that the more functional mechanical metamaterial with flexible behavior under tension, compression, or bending load could be designed and developed based on the present work.

CRediT authorship contribution statement

Peng Weitao: Investigation, Formal analysis. **Li Xiang:** Writing – original draft, Formal analysis, Data curation, Conceptualization. **Fan Rong:** Validation, Methodology, Formal analysis. **Lu Yang:** Writing – review & editing, Supervision, Project administration, Funding acquisition.

Declaration of Competing Interest

The authors declare that they have no known competing financial interests or personal relationships that could have appeared to influence the work reported in this paper.

Acknowledgments

This work is financially supported by the National Natural Science Foundation of China (Grant no. 12102193) and the Research Grants Council (RGC) Collaborative Research Fund (CRF) project C7074-23GF.

Appendix A. Supporting information

Supplementary data associated with this article can be found in the online version at doi:10.1016/j.eml.2025.102351.

Data availability

No data was used for the research described in the article.

References

[1] C. Huang, L. Chen, Negative Poisson's ratio in modern functional materials, Adv. Mater. 28 (37) (2016) 8079–8096.
[2] H.M. Kolken, A.A. Zadpoor, Auxetic mechanical metamaterials, RSC Adv. 7 (9) (2017) 5111–5129.
[3] K.E. Evans, A. Alderson, Auxetic materials: functional materials and structures from lateral thinking!, Adv. Mater. 12 (9) (2000) 617–628.
[4] J.I. Lipton, R. MacCurdy, Z. Manchester, L. Chin, D. Cellucci, D. Rus, Handedness in shearing auxetics creates rigid and compliant structures, Science 360 (6389) (2018) 632–635.
[5] G. Choi, L.H. Dudte, L. Mahadevan, Programming shape using kirigami tessellations, Nat. Mater. 18 (9) (2019) 999–1004.
[6] M.R. Dudek, K.W. Wojciechowski, J.N. Grima, R. Caruana-Gauci, K.K. Dudek, Colossal magnetocaloric effect in magneto-auxetic systems, Smart Mater. Struct. 24 (8) (2015) 085027.
[7] X. Li, Z. Fan, R. Fan, Y. Lu, Two-dimensional mechanical metamaterials with bending-induced expansion behavior, Appl. Phys. Lett. 117 (1) (2020) 011904.
[8] Y. Prawoto, Seeing auxetic materials from the mechanics point of view: a structural review on the negative Poisson's ratio, Comput. Mater. Sci. 58 (2012) 140–153.
[9] I.G. Masters, K.E. Evans, Models for the elastic deformation of honeycombs, Compos. Struct. 35 (4) (1996) 403–422.
[10] L. Yang, O. Harrysson, H. West, D. Cormier, Mechanical properties of 3D re-entrant honeycomb auxetic structures realized via additive manufacturing, Int. J. Solids Struct. 69 (2015) 475–490.
[11] A. Spadoni, M. Ruzzene, Elasto-static micropolar behavior of a chiral auxetic lattice, J. Mech. Phys. Solids 60 (1) (2012) 156–171.
[12] X.N. Liu, G.L. Huang, G.K. Hu, Chiral effect in plane isotropic micropolar elasticity and its application to chiral lattices, J. Mech. Phys. Solids 60 (11) (2012) 1907–1921.
[13] C.W. Smith, J.N. Grima, K. Evans, A novel mechanism for generating auxetic behaviour in reticulated foams: missing rib foam model, Acta Mater. 48 (17) (2000) 4349–4356.
[14] N. Gaspar, X.J. Ren, C.W. Smith, J.N. Grima, K.E. Evans, Novel honeycombs with auxetic behaviour, Acta Mater. 53 (8) (2005) 2439–2445.
[15] J.N. Grima, R. Jackson, A. Alderson, K.E. Evans, Do zeolites have negative Poisson's ratios? Adv. Mater. 12 (24) (2000) 1912–1918.
[16] M. Taylor, L. Francesconi, M. Gerendás, A. Shanian, C. Carson, K. Bertoldi, Low porosity metallic periodic structures with negative Poisson's ratio, Adv. Mater. 26 (15) (2014) 2365–2370.
[17] A. Andrew, Negative Poisson's ratios from rotating rectangles, Cmst 10 (2) (2004) 137–145.
[18] X. Li, W. Peng, W. Wu, J. Xiong, Y. Lu, Auxetic mechanical metamaterials: from soft to stiff, Int. J. Extrem. Manuf. 5 (4) (2023) 042003.
[19] Y. Jiang, Z. Liu, N. Matsuhisa, D. Qi, W.R. Leow, H. Yang, X. Chen, Auxetic mechanical metamaterials to enhance sensitivity of stretchable strain sensors, Adv. Mater. 30 (12) (2018) 1706589.
[20] M. Razbin, R. Bagherzadeh, M. Asadnia, S. Wu, Recent advances in wearable electromechanical sensors based on auxetic textiles, Adv. Funct. Mater. (2024) 2409242.
[21] M. Kapnisi, C. Mansfield, C. Marijon, A.G. Guex, F. Perbellini, I. Bardi, M. M. Stevens, Auxetic cardiac patches with tunable mechanical and conductive properties toward treating myocardial infarction, Adv. Funct. Mater. 28 (21) (2018) 1800618.

[22] S. Han, E.J. Lee, B. Kim, S. Jung, S. Jeong, S.W. Kim, S.Y. Lee, High-performance dual-mode triboelectric nanogenerator based on hierarchical auxetic structure, ACS Energy Lett. 5 (11) (2020) 3507–3513.
[23] J. Liu, D. Yan, W. Pang, Y. Zhang, Design, fabrication and applications of soft network materials, Mater. Today 49 (2021) 324–350.
[24] K.I. Jang, H.U. Chung, S. Xu, C.H. Lee, H. Luan, J. Jeong, J.A. Rogers, Soft network composite materials with deterministic and bio-inspired designs, Nat. Commun. 6 (1) (2015) 1–11.
[25] Q. Ma, H. Cheng, K.I. Jang, H. Luan, K.C. Hwang, J.A. Rogers, Y. Zhang, A nonlinear mechanics model of bio-inspired hierarchical lattice materials consisting of horseshoe microstructures, J. Mech. Phys. Solids 90 (2016) 179–202.
[26] L. Dong, C. Jiang, J. Wang, D. Wang, Design of shape reconfigurable, highly stretchable honeycomb lattice with tunable Poisson's ratio, Front. Mater. (2021) 191.
[27] J. Liu, Y. Zhang, Soft network materials with isotropic negative Poisson's ratios over large strains, Soft Matter 14 (5) (2018) 693–703.
[28] Y. Chen, T. Li, F. Scarpa, L. Wang, Lattice metamaterials with mechanically tunable Poisson's ratio for vibration control, Phys. Rev. Appl. 7 (2) (2017) 024012.
[29] T. Li, X. Hu, Y. Chen, L. Wang, Harnessing out-of-plane deformation to design 3D architected lattice metamaterials with tunable Poisson's ratio, Sci. Rep. 7 (1) (2017) 8949.
[30] J. Liu, D. Yan, Y. Zhang, Mechanics of unusual soft network materials with rotatable structural nodes, J. Mech. Phys. Solids 146 (2021) 104210.
[31] Y. Tang, J. Yin, Design of cut unit geometry in hierarchical kirigami-based auxetic metamaterials for high stretchability and compressibility, Extrem. Mech. Lett. 12 (2017) 77–85.
[32] Y. Tang, G. Lin, L. Han, S. Qiu, S. Yang, J. Yin, Design of hierarchically cut hinges for highly stretchable and reconfigurable metamaterials with enhanced strength, Adv. Mater. 27 (44) (2015) 7181–7190.
[33] X. Li, R. Fan, Z. Fan, Y. Lu, Programmable mechanical metamaterials based on hierarchical rotating structures, Int. J. Solids Struct. 216 (2021) 145–155.
[34] N. An, A.G. Domel, J. Zhou, A. Rafsanjani, K. Bertoldi, Programmable hierarchical kirigami, Adv. Funct. Mater. 30 (6) (2020) 1906711.
[35] K.K. Dudek, J.A.I. Martínez, G. Ulliac, M. Kadic, Micro-Scale Auxetic Hierarchical Mechanical Metamaterials for Shape Morphing, Adv. Mater. 34 (14) (2022) 2110115.
[36] D. Attard, J.N. Grima, A three-dimensional rotating rigid units network exhibiting negative Poisson's ratios, Phys. Status Solidi (b) 249 (7) (2012) 1330–1338.
[37] L. Cabras, M. Brun, A class of auxetic three-dimensional lattices, J. Mech. Phys. Solids 91 (2016) 56–72.
[38] B.A. Rogers, M.D. Valentine, A.J. Lunt, E.C. Pegg, V. Dhokia, Optimization and experimental validation of 3D near-isotropic auxetic structures, Mater. Des. 229 (2023) 111844.
[39] H.H. Huang, B.L. Wong, Y.C. Chou, Design and properties of 3D-printed chiral auxetic metamaterials by reconfigurable connections, Phys. Status Solidi (b) 253 (8) (2016) 1557–1564.
[40] Y. Xu, Y. Huang, H. Yan, Z. Gu, T. Zhao, R. Zhang, L. Jiang, Sunflower-pith-inspired anisotropic auxetic mechanics from dual-gradient cellular structures, Matter 6 (5) (2023) 1569–1584.
[41] Q. Hu, G. Lu, K.M. Tse, Compressive and tensile behaviours of 3D hybrid auxetic-honeycomb lattice structures, Int. J. Mech. Sci. 263 (2024) 108767.
[42] R. Gatt, M.V. Wood, A. Gatt, F. Zarb, C. Formosa, K.M. Azzopardi, J.N. Grima, Negative Poisson's ratios in tendons: an unexpected mechanical response, Acta Biomater. 24 (2015) 201–208.
[43] D. Yan, J. Chang, H. Zhang, J. Liu, H. Song, Z. Xue, Y. Zhang, Soft three-dimensional network materials with rational bio-mimetic designs, Nat. Commun. 11 (1) (2020) 1180.
[44] J. Hwang, J. Son, J.Y. Zhang, A. Janotti, C.G. Van de Walle, S. Stemmer, Structural origins of the properties of rare earth nickelate superlattices, Phys. Rev. B 87 (6) (2013) 060101.
[45] K. Bertoldi, P.M. Reis, S. Willshaw, T. Mullin, Negative Poisson's ratio behavior induced by an elastic instability, Adv. Mater. 22 (3) (2010) 361–366.
[46] A. Slann, W. White, F. Scarpa, K. Boba, I. Farrow, Cellular plates with auxetic rectangular perforations, Phys. Status Solidi (b) 252 (7) (2015) 1533–1539.
[47] J.N. Grima, L. Mizzi, K.M. Azzopardi, R. Gatt, Auxetic perforated mechanical metamaterials with randomly oriented cuts, Adv. Mater. 28 (2) (2016) 385–389.
[48] W. Miller, P.B. Hook, C.W. Smith, X. Wang, K.E. Evans, The manufacture and characterisation of a novel, low modulus, negative Poisson's ratio composite, Compos. Sci. Technol. 69 (5) (2009) 651–655.
[49] D. Mousanezhad, S. Babaee, H. Ebrahimi, R. Ghosh, A.S. Hamouda, K. Bertoldi, A. Vaziri, Hierarchical honeycomb auxetic metamaterials, Sci. Rep. 5 (1) (2015) 1–8.
[50] J. Zhou, J. Chang, X. Song, Z.Y. Li, L.Y. Zhang, H. Li, C. Zhang, Bio-inspired design and unusual mechanical properties of 3D horseshoe-shaped soft network metamaterials, Compos. Part B: Eng. 275 (2024) 111284.
[51] S. Babaee, J. Shim, J.C. Weaver, E.R. Chen, N. Patel, K. Bertoldi, 3D soft metamaterials with negative Poisson's ratio, Adv. Mater. 25 (36) (2013) 5044–5049.
[52] F. Warmuth, F. Osmanlic, L. Adler, M.A. Lodes, C. Körner, Fabrication and characterisation of a fully auxetic 3D lattice structure via selective electron beam melting, Smart Mater. Struct. 26 (2) (2016) 025013.
[53] D. Qi, P. Zhang, W. Wu, K. Xin, H. Liao, Y. Li, R. Xia, Innovative 3D chiral metamaterials under large deformation: theoretical and experimental analysis, Int. J. Solids Struct. 202 (2020) 787–797.
[54] T. Park, Y. Jang, D. Ahn, Y. Lee, Y. Kwak, J. Kim, Wave propagation-based characterization of 3D-printed soft auxetic structures, Compos. Struct. (2025) 118874.
[55] L. Yang, O. Harrysson, H. West, D. Cormier, Compressive properties of Ti–6Al–4V auxetic mesh structures made by electron beam melting, Acta Mater. 60 (8) (2012) 3370–3379.
[56] E.A. Friis, R.S. Lakes, J.B. Park, Negative Poisson's ratio polymeric and metallic foams, J. Mater. Sci. 23 (1988) 4406–4414.
[57] Y. Gao, Z. Zhou, H. Hu, J. Xiong, New concept of carbon fiber reinforced composite 3D auxetic lattice structures based on stretching-dominated cells, Mech. Mater. 152 (2021) 103661.
[58] X. Li, J. Chen, X. Feng, R. Fan, S. Lan, Y. Lu, Nature-inspired plate-based metamaterials with negative poisson's ratio and ultrahigh stiffness, J. Appl. Mech. 92 (6) (2025) 061006.